This document is downloaded from DR-NTU (https://dr.ntu.edu.sg)
Nanyang Technological University, Singapore.

Control of Methylene Blue Photo-Oxidation Rate over Polycrystalline Anatase TiO2 Thin Films via Carrier Concentration

Ong, S. W. Daniel; Lin, Jianyi; Seebauer, Edmund G.

2015

Ong, S. W. D., Lin, J., & Seebauer, E. G. (2015). Control of methylene blue photo-oxidation rate over polycrystalline anatase TiO2 thin films via carrier concentration. The Journal of Physical Chemistry C, 119(21), 11662-11671.

https://hdl.handle.net/10356/82766

https://doi.org/10.1021/acs.jpcc.5b01852

© 2015 American Chemical Society. This is the author created version of a work that has been peer reviewed and accepted for publication by Journal of Physical Chemistry C, American Chemical Society. It incorporates referee’s comments but changes resulting from the publishing process, such as copyediting, structural formatting, may not be reflected in this document. The published version is available at: [http://dx.doi.org/10.1021/acs.jpcc.5b01852].

Downloaded on 13 Jul 2024 20:28:32 SGT

Control of Methylene Blue Photo-Oxidation Rate over Polycrystaline Anatase TiO_2 Thin Films via Carrier Concentration

S. W. Daniel Ong,[‡] Jianyi Lin,[d] Edmund G. Seebauer[†*]

[†]Department of Chemical and Biomolecular Engineering, University of Illinois at Urbana-Champaign, Urbana, IL 61801, USA

[‡]Institute of Chemical and Engineering Sciences, Jurong Island, Singapore 627833, Singapore

[d]Nanyang Technological University, Singapore, Singapore 639798, Singapore

Band-bending, Photocatalysis, TiO_2, film, Defect engineering, Band engineering

ABSTRACT: Reaction rates on photocatalytic surfaces would often benefit greatly if minority photocarriers could be driven more efficiently to the surface through the manipulation of electric fields within the semiconductor. Such field-induced manipulation of photocurrent is commonplace in conventional optoelectronics, but translation to photochemistry and photoelectrochemistry has lagged. The present work demonstrates quantitatively that manipulation of the spatial extent of band bending via background carrier concentration can increase photoreaction rates by a factor of five or more in the case of methylene blue photodegradation over thin-film polycrystalline anatase TiO_2. A quantitative photocurrent model fits closely to experimental rate data with no adjustable parameters.

▪ INTRODUCTION

Thin-film semiconducting photocatalysts currently find applications in self-cleaning windows and other weather-exposed surfaces,[1,] and in anti-microbial[3] and anti-fouling coatings.[4] Reaction rates on these surfaces would often benefit greatly if minority photocarriers could be driven more efficiently to the

surface[5] through the manipulation of electric fields within the semiconductor. Such field-induced manipulation of photocurrent is commonplace in conventional optoelectronics, but translation to the specialties of photochemistry and photoelectrochemistry has lagged considerably. In these latter contexts, studies of near-surface band-bending have been reviewed[6] and have focused mostly on the effects of externally applied fields,[7,8] adsorption,[9] particle size,[10-13] metal deposition,[6] crystallographic orientation[14] and surface reconstruction.[15] Yet in optoelectronics, the primary methods for manipulating photocurrent involve the control of background carrier concentration and the use of semiconductor heterostructures. Heterostructures have found limited use in photocatalysis,[16,17] partly because of the complexities of using polycrystalline wide-bandgap semiconductors with electrically active grain boundaries and partly because of the difficulty in controlling background carrier concentration reliably. This latter difficulty is especially pronounced because of challenges to carrier concentration metrology in wide bandgap materials,[31] a dearth of dopants having shallow donor or acceptor levels,[18] effects of poorly-controlled concentrations of native point defects serving as donors or acceptors,[19,20] and effects of charged defects at grain boundaries.[39] Although the need for defect engineering to resolve these issues is becoming better recognized,[21-23] progress on that front will undoubtedly take time. In the meantime, a quantitative demonstration remains lacking that manipulation of electric fields within a photocatalyst by conventional means (especially via background carrier concentration) can improve photoreaction rates. The present work fills that gap in the case of methylene blue (MB) photodegradation over polycrystalline anatase TiO_2 in thin-film form.

TiO_2 is a wide bandgap (3.2 eV) semiconductor that is commonly employed for photocatalysis[24,25] as well as other applications where band-bending is important, such as gas sensors.[26] Among TiO_2's special merits for these applications are low cost and non-toxicity.[27-29] The literature on MB photodegradation by TiO_2 is voluminous,[30-40] making this reaction a useful, well-characterized test case for unambiguously demonstrating phenomena that result from band manipulation. In the present work, we controlled the photocurrent primarily via the width of the space charge layer (SCL) near the thin-film surface, which

was in turn controlled through the background concentration of charge carriers. We varied the carrier concentration via film thickness,[18,41] exploiting the fact that the donor concentration N_D scales inversely with final growth thickness due to a progressive decrease in the interface area residing at grain boundaries that is available for accumulating excess charge. This effect felicitously avoids the need for extrinsic dopants, which engender complications that could affect reaction rates such as segregation to the surface.

The existing literature already recognizes the importance of near-surface electric fields to surface photoreactions. For example, Wilson and Idriss[14,15] demonstrated significant changes in acetic acid photodecomposition in response to manipulating the last-layer atomic arrangement of the rutile (001), which propagated into quantified changes in surface barrier height – and by implication, near-surface electric field. By contrast, the present work measures and manipulates N_D, and develops a quantitative photocurrent model that fits closely to rate data with no adjustable parameters.

METHODS

Photocurrent model. The basic approach of this work compares the variation of MB reaction rate vs. N_D with the corresponding variation predicted by a model for photocurrent. The following description of the photocurrent model assumes n-type material (which is true for the anatase used here), but analogous arguments can be made for p-type semiconductors in depletion. The polycrystalline anatase is approximated as a uniform medium. Grain boundaries are accounted for implicitly through their contribution to N_D and the minority carrier lifetime. As the experimental results will show, this approximation is remarkably accurate.

The reaction rate equals the mathematical product of the surface photocurrent and the likelihood P that a photocarrier arriving at the surface will induce a reaction event. The total rate of current flow J_{pc} of holes to the surface is given by the sum of drift (*i.e.*, electric-field driven) and diffusion components. Under steady-state conditions, the total photocurrent density of minority carriers to the surface is given by:[42]

1 $$J_{pc} = J_{dr} + J_{diff}$$

where J_{dr} and J_{diff} are the drift and diffusion current densities, respectively.

For a light-absorbing semiconductor in depletion (as opposed to accumulation or inversion) with spatially uniform N_D, the governing equation for the photocurrent induced by illumination is given by:[43]

2 $$J_{pc} = J_0\left(1 - e^{-\alpha W}\right) + J_0\left(\frac{\alpha L_p}{1+\alpha L_p} e^{-\alpha W}\right)$$

where

3 $$J_0 = \frac{qI(1-R)}{h\nu}$$

Here J_{pc} denotes the photocurrent, J_0 denotes the photocurrent with unit internal quantum efficiency, i.e. if all absorbed photons were converted into collected electron-hole pairs (EHPs), α is the absorption constant, L_p is the hole diffusion length, W is the width of the SCL, q is the elementary charge, I is the optical intensity, h is Planck's constant, R is the reflectance of the sample and ν is the frequency of the incident light. In equation 2, the first term in parentheses represents the drift component of the photocurrent, while the second term after the plus sign represents the diffusion component. The drift current is computed based on the assumption that the electric field within the SCL sweeps to the surface all minority charge carriers created by photons. This assumption is reasonable for the anatase used here, as detailed in the Methods section.

The exponential term $e^{-\alpha W}$ originates from the conventional depth dependence of photocarrier generation as the penetrating light is progressively attenuated by absorption. Equation 2 indicates that J_{pc} depends exponentially on the SCL width W. There are two distinct ways to control W: 1) variation of the bulk doping concentration/type (*i.e.,* the position of the bulk Fermi energy via N_D), and 2) variation of the surface potential V_S (*i.e.*, the position of the surface Fermi energy). W depends upon N_D and V_S according to:[44]

4 $$W = \sqrt{\frac{\varepsilon\varepsilon_0}{q}\frac{V_S}{N_D}}$$

where ε and ε_0 respectively denote the relative permittivity of the semiconductor and the permittivity of free space. Substitution of equation 4 into equation 2 and factoring out J_0 yields an explicit form for photocurrent that depends upon carrier concentration and the surface potential:

5 $$J_{pc} = J_0\left[1 - \frac{1}{1+\alpha L_p} e^{-\alpha\sqrt{\frac{\varepsilon\varepsilon_0}{q}\frac{V_S}{N_D}}}\right]$$

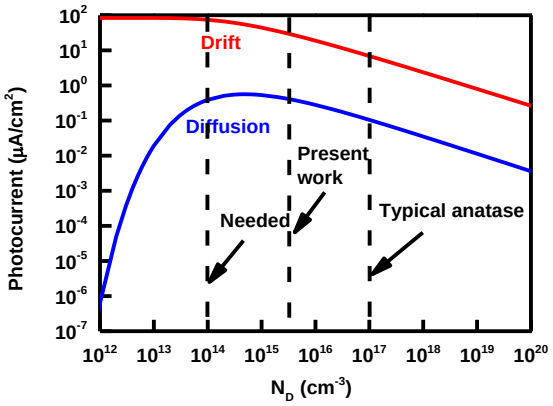

Figure 1. Comparison of drift and diffusion currents in thin-film anatase under 365 nm illumination. The contribution from the drift component dominates under all conditions.

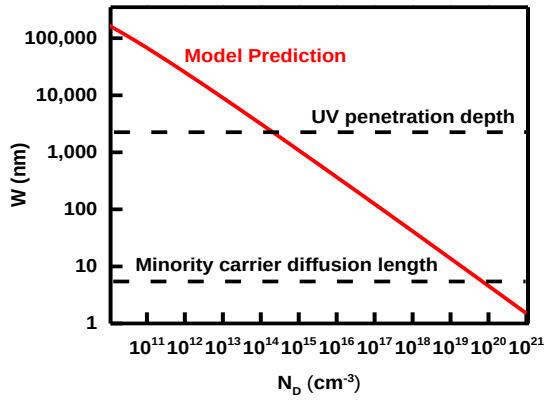

Figure 2. Predicted variation of the width *W* of the space charge layer in anatase with donor concentration N_D. Also shown are the penetration depth for light at 365 nm, as well as the estimated minority carrier diffusion length for the anatase.

Figure 1 shows the photocurrent's dependence on donor carrier concentration as computed with equation 5, with parameters for anatase estimated as detailed in the Methods section. The drift compenent of J_{pc} dominates for carrier concentrations that are typical of anatase.[18] Importantly, the drift compenent rises substantially as N_D decreases from this level down to about 10^{14} cm^{-3}. At this point, the drift component (and J_{pc}) has risen to a value roughly a factor of 30 above the "typical" level. A decrease in N_D leads to an increase in J_{pc} because the SCL width *W* increases as N_D declines, as indicated in equation 4 and shown in Figure 2. The penetration depth of the light is larger than *W*, and the minority carrier lifetime is sufficiently long for virtually all carriers to survive while traversing to the surface. Increasing *W* therefore increases the volume of semiconductor that can be harvested for minority carriers. The drift component plateaus at carrier concentrations below 10^{14} cm^{-3} because W has increased beyond the penetration depth of the light.

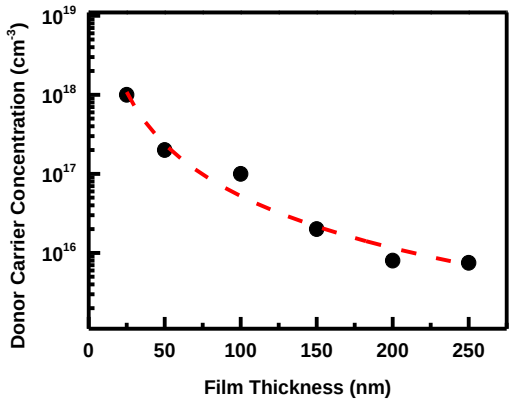

Figure 3. Variation of n-type carrier concentration for TiO_2,[41,40] prepared by the same methods used for this study. Carrier concentration was measured by capacitance-voltage techniques. [18] The line is a guide to the eye**.**

Variation of N_D with film thickness. To control the carrier concentration without using extrinsic dopants that can affect reaction rates due to surface segregation, we exploited the fact that the donor concentration N_D scales inversely with thickness in anatase as exemplified in Figure 3. Similar trends had been reported for other oxide materials such as ZnO and SnO_2.[45,46] In anatase, this variation originates from a progressive reduction in the surface area of grain boundaries.[18] Such boundary regions support electrically active defects[47] and serve as aggregation loci for charged point donor defects such as Ti interstitials and O vacancies.[48] Lowering the area of such boundaries therefore leads to a decrease in N_D.

Note that variations of photoreaction rate with TiO_2 film thickness are already well documented in literature.[49-53] The rate typically increases with film thickness up to a point, followed by a plateau at greater thicknesses that range widely from 140 nm to 5 μm. The usual interpretations presuppose that photocarriers migrate to the surface via diffusion. In this view, the volume over which light creates EHPs increases as the thickness increases, which in turn raises the photcatalytic rate. The rate ulimately plateaus because the thickness exceeds either the diffusion length of photocarriers or the penetration depth of the light. The present work interprets our rate variations in terms of carrier drift rather than diffusion. In all data presented here, the film thickness lies above the photocarrier diffusion length (~10 nm)[54] and below the penetration depth of the light (~1 μm at the usual wavelength λ=365 nm). The relevant volume of photocarrier generation is determined by neither the total film thickness nor the photocarrier diffusion length, but rather by the width W of the SCL. We control W via N_D, which we adjust indirectly via the film thickness. Although no plateau in rate is observed in the present experimental results, figure 2 predicts a plateau below 10^{14} cm^{-3}. The reason is that W exceeds the pentration depth of the light in this regime. This connection between rate and penetration depth fits well with the common explanation that beyond a film thickness greater than the diffusion length of the photogenerated EHPs, they will no longer reach the surface. In the present case, the transport mechanism of photocarriers to the surface differs considerably and allows for more facile rate manipulation via N_D and V_S.

Expermental Details. The TiO_2 anatase films were synthesized using atomic layer deposition as detailed elsewhere [41]. Briefly, films were grown on commercial n-type Si(100) (Sb, 0.013 Ω cm resistivity, 2 cm ×_2 cm) at 400°C. The precursors were $Ti(OCH(CH3)_2)_4$ (TTIP, Strem Chemicals Inc., 98%) and H_2O (deionized, no further purification), with N_2 (SJ Smith, 99.999%) serving as the carrier gas. A full growth cycle consisted of a TTIP pulse (8 s), N_2 purge (10 s), H_2O pulse (8 s), and another N_2 purge (10 s). Film thickness was determined by ellipsometry.

XPS was performed in an ultra-high vacuum system (base pressure ~10^{-10} mbar) using a Thermo VG Scientific ESCALAB 250 X-ray photoelectron spectrometer having a pass energy of 40 eV and a micro-focused, monochromated X-ray source (Al kα at 1486.6 eV). Energy resolution was 0.3 eV (full width at half-maximum). Specimens were secured to a stainless steel sample block with double-sided conducting adhesive copper tape. Data processing and analysis was accomplished using the software XPSPeak and its automatic fitting feature. The binding energy scale was referenced to the C 1s line of graphitic carbon, set at 284.6 eV. The relevant spectral regions were all fitted with Shirley backgrounds.

UPS was performed using a Thermo VG Scientific ESCALAB 250 spectrometer with a helium discharge lamp accessory. The lamp source provided He I ($h\nu$ = 21.2 eV) photons, and the energy scale was calibrated to a Ni reference. Specimens were biased for the He I spectra to induce narrowing in the secondary electron tail. Spectra for the TiO_2 specimens were referenced to the Fermi edge of clean Ni, and changes in workfunction were monitored via the relative difference between the secondary electron tails of the films and the Ni reference. Emited photoelectrons were collected normal to the surface.

BET was performed by conventional methods using a Micromeritics ASAP 2420 gas sorption analyzer on film specimens weighing about 0.25 g.

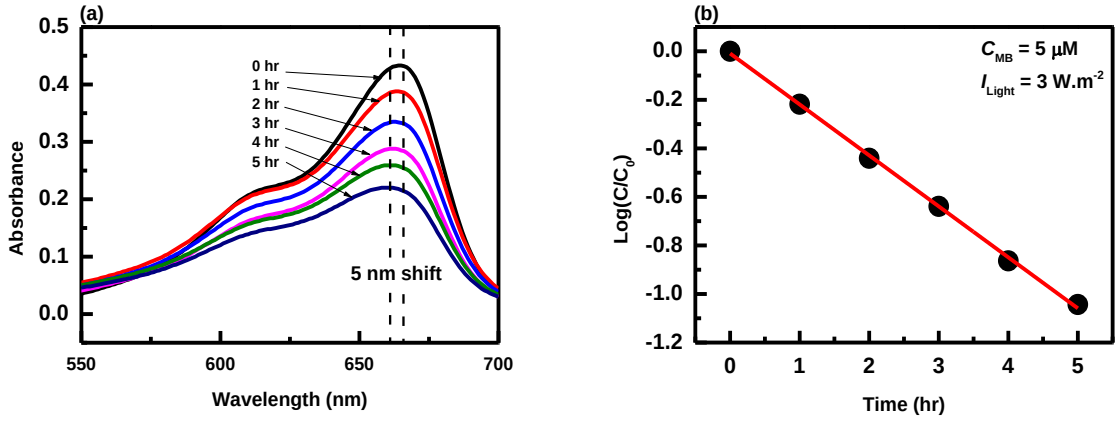

Figure 4. (a) UV-visible spectra of MB showing the absorbance before and after the photoreaction and (b) regression curve indicating that MB degradation is consistent with a pseudo-first-order rate equation. The intensity of the characteristic peak at 664 nm fell significantly after UV illumination. There was also a concomitant shift in the peak position from 664 nm to 654 nm, indicative of oxidative de-methylation.

XRD was performed at room temperature with a high-resolution Bruker D8 diffractometer operated at 45 kV and 40 mA with a Cu Kα1 primary x-ray beam (λ = 1.5406 Å). Data were taken over 2θ angles from 20° to 60°.

Photoreaction rate measurements were performed in a custom apparatus comprising a reaction vessel, a UV light source and a UV-visible spectrophotometer. The reaction vessel was a 25 mL flat-based beaker made with borosilicate glass. The vessel was wrapped with aluminum foil in order to confine light within the reaction vessel. A UVP Blak-Ray B-100 UV lamp served as the light source. The lamp housed a 100 W Sylvania H44GS-100M mercury spot light bulb emitting at a peak wavelength of 365 nm. A quartz window was attached to the top of the reaction vessel, and the specimen was laid at the bottom normal to the axis of the light source. UV light intensity was measured with a UVX digital radiometer coupled with the UVX-36 sensor. The radiometer had an error of ± 5%, and the sensor had been calibrated using 365 nm wavelength light. For all photocatalysis experiments, the incident intensity was 300 μW.cm^{-2}.

Optical absorption was monitored with a Shimadzu UV-3600 spectrophotometer. Quartz cuvettes with a path length of 1 cm were used to hold the reactant samples for spectrometry, with each cuvette

holding up to 3 mL of reactant. The UV-Vis spectrometer was controlled via a software interface (UVProbe version 2.33) which enabled the collection of raw data of absorbance vs. wavelength of light in the range of 200 to 800 nm. The MB was obtained from Acros MB hydrate pract. 75% (formula weight of 319.85 $gmol^{-1}$). Aqueous MB was prepared from a concentrated solution by dissolving 250 mg of hydrate in 1000 mL of deionized H_2O. (Automatic Sanitation Module, Millipore).

The photo-oxidation reaction was carried out batch-wise for 100 min with an initial MB concentration of 5 μM at pH 6.4. The kinetics obey a pseudo-first order rate equation [31-33,55] given by:

$$r = k_r C_{MB} C_{H^+}^{-0.08} \quad (6)$$

where r is the reaction rate, k_r is the apparent rate constant, C_{MB} is the concentration of MB, and CH+ is the hydronium ion concentration. C_{MB} was monitored via the conventional Beer-Lambert optical absorbance law. Figure 4 shows examples of optical absorbance data taken over time, together with resulting concentrations plotted in standard semilogarithmic form. In line with published literature, the initial absorbance peak at 664 nm shifted continuously over time to 654 nm, consistent with degradation via oxidative de-methylation.[31] However, for concentration measurements, the absorbance was always monitored at 664 nm. Typical MB conversions over 100 min ranged from 20 to 80%.

Determination of Material Parameters in the Photocurrent Model. The values of α and the band gap E_g were obtained through optical absorption measurements. Numerous values for α and E_g can be found in the literature[56-60] (examples shown in Table 1), but the values vary substantially with synthesis method. We therefore measured these values directly.

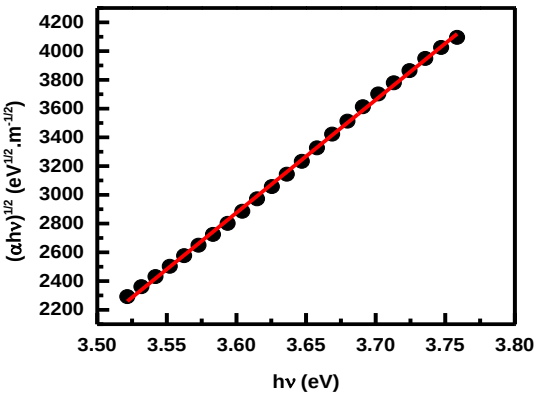

Figure 5. Fitting of equation 7 near the absorption edge at 365 nm. E_g was calculated from the slope and intercept of the linear regression.

Table 1: Values of α and E_g obtained from plots of $(\alpha h\nu)^{1/2}$ vs. $h\nu$ for a selection of five different synthesis methods.

Ref.	Synthesis	α (m^{-1})	E_g (eV)
[56]	MOCVD	9.42×10^5	3.21
[57]	Sol-gel Spin	1.60×10^6	3.56
[58]	PLD	2.13×10^6	3.22
[59]	RF Sputtering	3.56×10^5	3.34
[60]	ALD	2.10×10^6	3.12

The absorption coefficient near the band edge for indirect allowed transitions can be expressed as:[61]

$$\alpha = \frac{A\left(h\nu - E_g\right)^2}{h\nu} \qquad (7)$$

where A is the experimental absorption constant obtained via Beer's Law. The value of α was determined experimentally using UV-visible spectroscopy in absorbance mode. TiO_2 films of varying thicknesses were probed, and data for A vs. absorbance wavelength obtained, from which the value of α was directly calculated. The data were subsequently fitted near the absorption edge at 365 nm (Figure 5) using equation 7 to extract the E_g through the slope and intercept of a linear regression. The average values of α and E_g obtained this way were 6.93×10^5 m^{-1} and 3.24 eV respectively.

Following the suggestion of Butler for TiO_2,[43] the minority carrier diffusion length L_p was approximated with the assumption of a diffusion-controlled bulk recombination process. Within this framework, L_p obeys:

$$L_p = \left(\frac{\mu_p}{\mu_p + \mu_e} \right)^{1/2} \left(\frac{\varepsilon \varepsilon_0 kT}{4\pi q^2 N_D} \right)^{1/2} \quad (8)$$

where μ_e and μ_p respectively denote the mobility of electrons and holes. The calculated value of L_p is in the range of 10 nm, assuming that the electron and hole mobilities equal each other.[62] The value of ε was set to be 55.[63] In the photocurrent model, L_p appears in the compound term αL_p (equation 5). The exact value of L_p is not too crucial to the calculation of J_{pc} because $\alpha L_p << 1$.

The drift distance of holes is needed to justify the assumption that the electric field $\mathscr{E}$ within the SCL sweeps to the surface all minority charge carriers created by photons. The drift distance can be estimated from the product of the drift velocity $\mu_p \mathscr{E}$ and the carrier lifetime. $\mathscr{E}$ was taken to be its average value within the SCL, given by equation 4, while μ_p was taken to be 1×10^{-4} $m^2V^{-1}s^{-1}$[64] (following the assumption that $\mu_p = \mu_e$). The hole lifetime varies with the concentration of recombination centers in the material, but has been found for anatase to be in the tens of ns range (~50 ns)[65]. The drift distance that results is in the range of 1 – 10 μm, far exceeding the thickness of the films examined here. Note that in all the experiments, W is always contained entirely within the film thickness, although W = 282 nm lies just below the thickness for the 300nm films.

- **RESULTS**

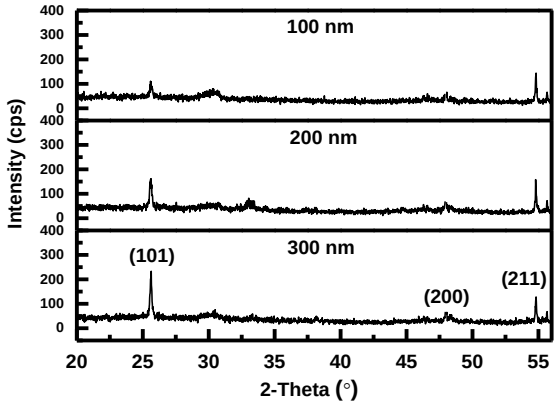

Figure 6. XRD patterns for 100, 200 and 300 nm films. The key peaks match the (101), (211) and (200) orientations of anatase.

Crystalline Phase. Figure 6 shows X-ray diffraction (XRD) patterns for films with thicknesses of 100, 200 and 300 nm films. The spectra match well with the anatase phase of TiO_2. The lines corresponding to the (101) and (200) directions intensify with thickness, which implies improved long range ordering for these orientations. Application of the Scherrer equation yields a crystallite size of ~50 nm that remains essentially independent of thickness.

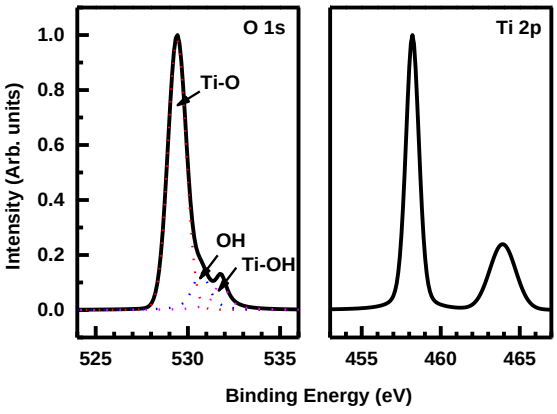

Figure 7. XPS spectra of a representative 300 nm film sample. The left spectrum shows the O 1s feature, with the dominant peak at 530 eV (metallic oxide). The other peaks are assigned to OH groups at bridging

sites or Ti-OH. The right spectrum shows the Ti 2p feature. The Ti $2p_{3/2}$ peak areas are in the expected 2:1 ratio with the Ti $2p_{1/2}$ peak, with the dominant peak belonging to Ti^{4+}.

Film Composition. Figure 7 shows the XPS O 1s and Ti 2p features for a representative 300 nm film sample. All O 1s spectra show distinct peak contributions at higher binding energy positions relative to the main peak at 529.7 eV. These higher binding energy peaks represent OH groups existing as Ti-OH (533.5 eV) or OH at bridging sites (531.5 eV). [66-69] The Ti 2p peaks comprising Ti $2p_{3/2}$ and Ti $2p_{1/2}$ are located at 458.5 eV and 464.2 eV respectively, with a peak separation of 5.7 ± 0.07 eV. The Ti peak positions indicate an oxidation state of Ti^{4+}. The lack of shoulders or even asymmetry in the peaks suggests that little or no Ti^{3+} is present. Film thickness variations yeilded no significant variation in peak shape or broadening. Figure 8 shows the O to Ti ratio calculated from the areas of the O 1s and Ti 2p peaks. The ratio nominally averages slightly over 2.0, and does not vary appreciably with film thickness.

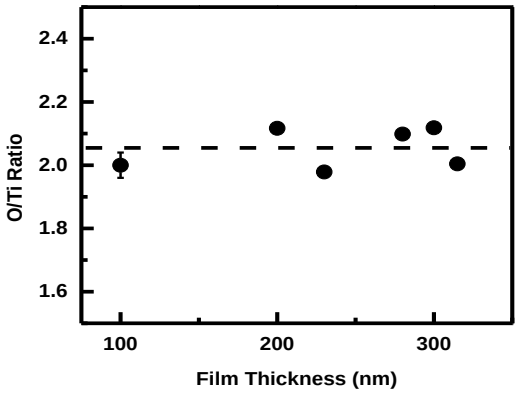

Figure 8. The ratio of O to Ti from XPS as a function of film thickness. No appreciable variation is observed. The line represents a guide to the eye.

Porosity. The Brunauer-Emmet-Teller (BET) and the Barrett-Joyner-Halenda (BJH) methods were used to probe whether reaction-accessible void volumes exist within the bulk matrix of the films. A non-porous Si wafer was employed for reference measurements. The results showed that no significant void volumes are accessible to reactants, so that photocatalytic rates occur entirely on the exposed surface of the anatase.

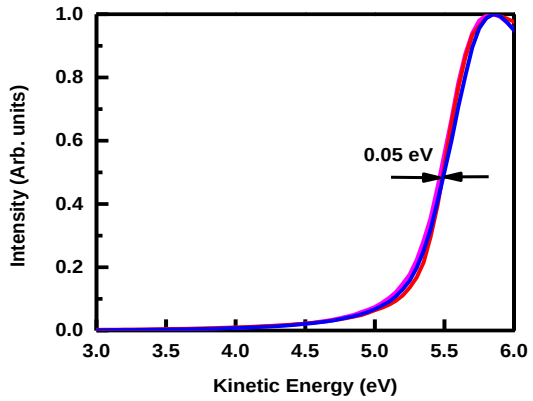

Figure 9. Secondary electron tail for 100, 200 and 300 nm films. These He I UPS spectra indicate that the workfunction for the films change little with thickness – to within 0.05 eV.

Workfunction Measurement. Figure 9 shows secondary electron tails for He I (21.2 eV) ultraviolet photoelectron spectroscopy (UPS) of the films in the range 100-300 nm. The tails exhibit a small 0.05 eV spread in workfunction, but with no particular trend. The average surface workfunction is 5.45 ± 0.025 eV.

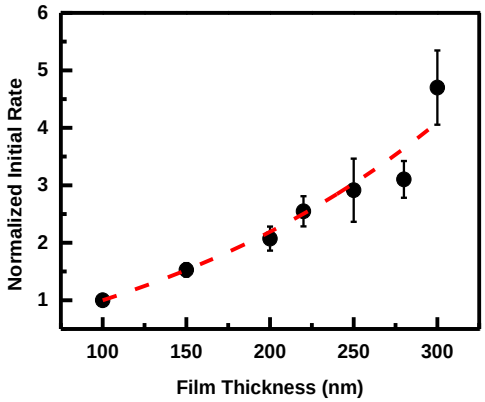

Figure 10. Initial MB photodegradation rates rates plotted against film thickness. Rates are normalized to the value at 100 nm. Line represents a guide to the eye.

Methylene Blue Degradation Rate. Figure 10 shows the initial rates of MB photodegradation, plotted as a function of film thickness. For convenience, the rates have been normalized to the rate of the 100 nm film, which degraded MB at an initial rate of 0.14 $\mu M.hr^{-1}.cm^{-2}$ for an initial MB concentration

of 5 μM. Assuming that every surface site (with area density ~10^{15} cm^{-2}) is capable of photocatalysis, this rate corresponds to a turnover frequency of 1.2×10^{-4} s^{-1}. The rate increases by nearly a factor of five as the thickness increases from 100 to 300 nm.

The quantum yield, *QY* for the films can be calculated through the relation:

$$QY = \frac{r_0}{I} \tag{9}$$

where r_0 is the initial degradation rate of MB. The *QY* ranges from 2.2×10^{-4} for 100 nm films to 1.0×10^{-3} for 300 nm films. The reaction probability *P* of photocarriers that reach the surface obeys:

$$P = \frac{r_0}{J_{PC}} \tag{10}$$

The value of J_{pc} was estimated using equation 2, and the average value of the reaction probability computed this way is 0.0021 ± 0.0002.

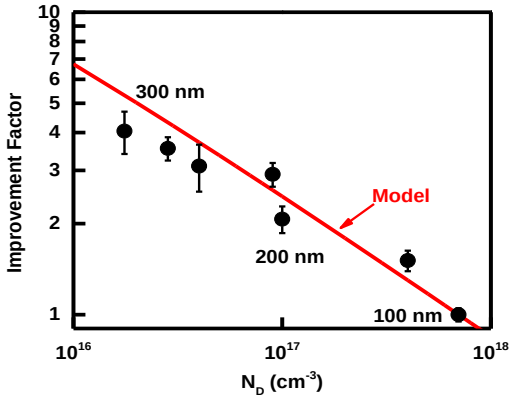

Figure 11. Improvement factor vs carrier concentration for experimental rate data (Figure 10) and predicted J_{pc} (Figure 1), scaled to the corresponding values at a thickness of 100 nm. Rate data closely track the predictions for J_{pc}.

Figure 11 shows a log-log plot of the same rate data plotted vs N_D, with the vertical axis showing an "improvement factor" for both experimental data and model predictions scaled to the corresponding

values at a thickness of 100 nm. The horizonal scale shows thicknesses in Figure 10 converted to N_D via the graph in Figure 3. The rate data closely track the predictions for J_{pc}. Note that equation 5 for J_{pc} does not predict absolute experimental rates directly, since that prediction would presuppose *a priori* knowledge of *P*. However, the model does permit *a priori* comparison of improvement factors.

- **DISCUSSION**

Figure 12 shows the band scheme for n-type anatase TiO_2 employed in this work. The Fermi level within the bulk of semiconducting anatase obeys:

$$E_F = E_i + kT \ln \frac{n_0}{n_i} \qquad (11)$$

where E_i is the intrinsic level, k is the Boltzmann constant, T is the temperature, n_0 is the measured charge carrier density, and n_i is the charge carrier density of the intrinsic semiconductor (with no dopants or electrically ionized native defects). We used the following parameter values that are typical for TiO_2: n_i = ~10^{-7} cm^{-3}, $n_0 = N_D$ (~10^{16} - 10^{18}) and $E_i = E_V + 1.62$ eV. These parameters yield the Fermi energy in the bulk as $E_F = E_V + 3.09$ eV to $E_V + 2.99$ eV. The Fermi level at the surface, E_{FS} was obtained via UPS, and gave a value of $E_{FS} = E_C - 0.66$ eV. This value remained constant with variations in film thickness (and therefore variations in N_D). The difference $q_{VS} = E_{FS} - E_F$ yields a range for V_S between 0.41 and 0.51 V.

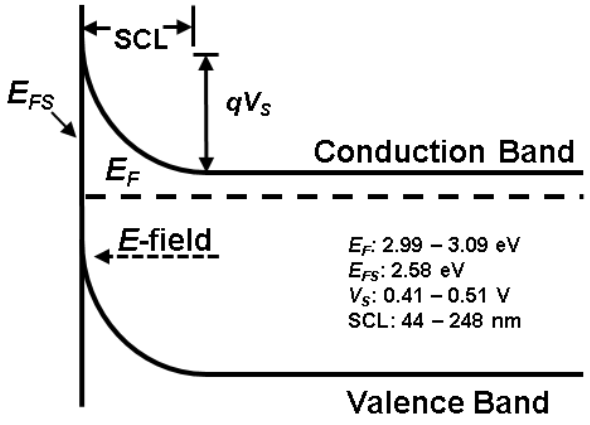

Figure 12. Band scheme for the n-type anatase employed in this work. Diagram assumes that the polycrystalline material acts as a uniform medium. Numerical values for various parameters are shown inset. Fermi levels are referenced from the valence band maximum.

Assessment of the Photocurrent Model. The correspondence in

Figure 11 between the experimentally measured improvement factor for the experimentally measured rates and the predictions of the drift-based photocurrent model is remarkably good, especially considering that the model contains no adjustable parameters – all parameters of the model were either measured or derived from literature.

A comparison of the photocurrent model with the experimental result by Wilson and Idriss [15] is particularly relevant. They examined the effect of crystallographic orientation of single crystal TiO_2, and suggested that changes in the quantum yield of acetic acid decomposition resulted from fixed charge accumulation at the surface due to the local atomic coordination. They reported a change in quantum yield of 2.5 times between the {001} and {11ose facets, comparable to the 2.7 times predicted by the photocurrent model applied to the data they report.

Reaction Probability. The value of the reaction probability near 0.2% is in line with those reported in the literature. Houas et al[32] reported values of 0.12% and 0.14% for 290 nm and 340 nm light respectively for his study on MB degradation, and Matthews reported a value close to 0.1%.[36] The rate limiting step of this reaction under present conditions is the conversion of water by photogenerated holes to OH radicals.[70] The value of *P* comprises many factors, including the efficiency of hole transfer to OH^- and the rate of electron-hole recombination at the surface. The hole transfer efficiency depends upon surface attributes such as the presence of segregated impurities and the average crystallographic orientation of the anatase, while the recombination rate depends upon these as well as other factors such as the presence of supported metal particles and the concentration of adsorbed OH^-.

The films used in this study are undoped and chemical analysis via XPS reveals strong Ti 2p and O 1s peaks, with an example shown in Figure 7. Prior analysis of the carbon content in the bulk suggests a carbon concentration of less than 0.2 at.%.[18] As such, we assume that chemical impurities play little to no part in our investigation.

Further Prospects for Improving Photocatalytic Rate. In principle, V_S can also serve as an independent variable for controlling J_{pc} via E_{FS}. Equation 5 shows the variation in J_{pc} to be expected. E_{FS} is constant in the present work, probably due to Fermi level pinning. However, surface treatments of various kinds can alter the density of states, as has been demonstrated in other semiconductor systems.[71-73]

Ridding the TiO_2 of more charged defects could conceivably decrease the carrier concentration from 10^{17} to 10^{14} cm^{-3}. J_{pc} would then increase from about 5 μA cm^{-2} to 100 μA cm^{-2} which translates to ~10^{14} cm^{-2} s^{-1} extra charges; this represents an increase by a factor of about 20. If every photocarrier were to stimulate a chemical reaction event, this photocurrent would be equivalent to roughly one hundredth of a monolayer per second, or a catalytic TOF of about 0.1 s^{-1}.

Relation to Particulate Photocatalysts. Particulate photocatalysts present an important application, as many commercial photocatalysts are synthesized in particulate form and subsequently pelletized. For these particulate catalysts, the nominal SCL is much larger than the particle diameter and the degree of band-bending is also much weaker, in which case diffusion is the dominating mechnism for J_{pc}. With a hole diffusion length of 10 nm and grain diameters of typically ~20 nm, band-engineering could start to make a difference in charge promotion to the particle surface. If the particles are sintered to a good degree for electrical contact, the particle network may then support the electric fields in a way similar to the grains in a film, and band-bending could be used to manipulate the performance of the catalyst. That said, the effect from band-bending wouldn't be felt if the catalysts interact with strong electrolytes where the potential everywhere is set by the redox couples within the solution.

The photocurrent model should apply to particulate catalysts, given a means to accurately determine and change parameters such N_D and V_S. Albery and Bartlett [74] developed the potential distribution in a spherical n-type semiconductor particle based on the Poisson-Boltzmann distribution. The band bending is given by

$$12\ V_S = \frac{kT}{6}\left(\frac{r-(r_0-W)}{L_D}\right)^2\left(1+\frac{2(r_0-W)}{r}\right)$$

where r is the distance from the center, r_0 is the radius of the particle, and L_D is the Debye length given by $L_D = (\varepsilon kT/q^2N_D)^{1/2}$.

For particles with radii much bigger than W, the degree of band bending is given by $V_S=qN_DW^2/2\varepsilon$, which is equivalent to equation 4, while that for small particles can be expressed by $V_S=qr^2N_D/6\varepsilon$. There is a drive toward smaller catalyst particles in order to take advantage of the increased surface area for catalysis, and in such cases, the key parameters to manipulate would be the relative permittivity of the material, charge carrier concentration and the actual size of the particle. A promising material with high relative permittivity can be found in tantalum oxynitride,[75] where it had exhibited stability in aqueous media, as well as the ability to function well under visible light.[76] A key feature of this material is the ability to tune its optical properties through varying the oxygen content relative to nitrogen, with a range of bandgap from 1.85 – 4.0 eV possible.[75] Application of tantalum oxynitride to photocatalytic water splitting had also been demonstrated by Higashi et al, where highly stable water splitting over visible light was observed.[77]

Implication for Photocatalytic Water Splitting. Photocatalytic water splitting involves the decomposition of water through EHP mediated reactions for the primary purpose of producing H_2 and the literature is replete with studies on the use of TiO_2 as the catalyst. The suitability of TiO_2 for water splitting is due to its bandgap ($\geq$ 1.23 eV), conduction and valence band positions for the reduction and oxidation reactions with water to take place, as well as its stability in aqueous media. A common strategy to improve the performance of water splitting catalysts involves the use of noble metals such as Pt to "trap" the

photoelectrons generated in the conduction band, leaving the holes behind to prevent recombination. Studies on water splitting usually place emphasis on the photoelectrons since the reduction of water is directly related to the production of H_2. This is in contrast to air/water purification where photoholes are the main initiators for the degradation of hydrocarbon based pollutants. Nada et al[78] showed qualitatively that the addition of electron donors such as methanol and lactic acid enhanced H_2 production during photocatalytic water splitting, while Li et al[79] used pollutants such as oxalic acid and formaldehyde to demonstrate that photocatalytic degradation of the pollutants can be integrated with H_2 production, with H_2 production being enhanced when the pollutant species acted as hole scavengers. In the current work, the implementation of band-engineering to improve hole supply for hydrocarbon oxidation will be accompanied by an equal increase in the electron supply available for the reduction of water. In this way, it is conceivable that H_2 production rates through photocatalytic water splitting could be significantly enhanced.

- **CONCLUSION**

Photocatalysts resemble conventional optoelectronic devices in certain important respects. In both cases, the semiconductor interacts with light via absorption or emission, and the efforts to develop improved photocatalysts have accordingly focused heavily on bandgap engineering to improve solar light absorption.[80-82] However, performance also benefits in both cases by directing carrier flow via intentional manipulation of internal electric fields. Although manipulation of such fields is standard practice for the design and fabrication of optoelectronics, such methods are much rarer in the design of photocatalysts – even in thin film form. The semiconductor band engineering required for such manipulation is presently difficult for several reasons. Band occupation (as represented by carrier concentation) is difficult to measure[39] and control[18] in wide bandgap oxides. Control is complicated by the existence of large numbers of charged native defects having complicated defect chemistry[19,20]. Band shape near surfaces or interfaces is also difficult to measure and control, as oxide surface and interfaces typically support electrically active defects of varying amounts and types that depend sensitively on ambient conditions and synthesis

conditions. In other words, successful band engineering requires significant defect engineering both within the semiconductor bulk and at surfaces and interfaces. The importance of such defect engineering for photocatalysis has been recognized previously,[21,22] but standard practices developed in the microelectronics industry [221,22,83-85] have diffused relatively slowly into the design of photocatalysts.[21] The present work represents a modest step in that direction.

In this work, the photocurrent model was used to predict changes in reaction rates through hole-mediated reactions with MB photo-oxidation as a model. Although the degradation of MB is initiated by OH radicals, it is reasonable to believe that reactions initiated directly by hole attack on the model species will be affected in a similar manner. Future studies on such systems, as well as anaerobic reactions involving photo-reduction (e.g. degradation of azo dyes) will also add to the on-going discussion in this field.

▪ AUTHOR INFORMATION

Corresponding Author

eseebaue@illinois.edu

Author Contributions

All authors have given approval to the final version of the manuscript.

Notes

The authors declare no competing financial interests.

▪ ACKNOWLEDGMENT

This work was supported by NSF (DMR 10-05720 and 13-06822) and Singapore's Agency for Science, Technology and Research.

- **ABBREVIATIONS**

BET, Brunauer-Emmet-Teller; BJH, Barrett-Joyner-Halenda; EHP, electron-hole pairs; MB, methylene blue; SCL, space charge layer; UPS, ultraviolet photoelectron spectroscopy; UV, ultraviolet; XRD, X-ray diffraction; XPS, X-ray photoelectron spectroscopy

- **REFERENCES**

(1) Fujishima, A.; Hashimoto, K.; Watanabe, T. *TiO_2 Photocatalysis: Fundamentals and Applications*; BKC: Tokyo, 1999.

(2) Paz, Y.; Luo, Z.; Rabenberg, L.; Heller, A. Photooxidative Self-Cleaning Transparent Titanium Dioxide Films on Glass, *J. Mater. Res.* **1995**, *10*, 2842-2848

(3) Chung, C. J.; Lin, H. I.; Tsou, H. K.; Shi, Z. Y.; He, J. L. An Antimicrobial TiO_2 Coating for Reducing Hospital-Acquired Infection, *J. Biomed. Mater. Res. B* **2008**, *85B*, 220-224

(4) Wang, Y.; Wang, L. L.; Liu, M. Y. Antifouling and Enhancing Pool Boiling by TiO_2 Coating Surface in Nanometer Scale Thickness, *AIChE J* **2007**, *53*, 3062-3076

(5) Takahashi, M.; Tsukigi, K.; Uchino, T.; Yoko, T. Enhanced Photocurrent in Thin Film TiO_2 Electrodes Prepared by Sol–Gel Method, *Thin Solid Films* **2001**, *388*, 231-236

(6) Zhang, Z.; Yates, J. T. Band Bending in Semiconductors: Chemical and Physical Consequences at Surfaces and Interfaces, *Chem. Rev.* **2012**, *112*, 5520-5551

(7) Jiang, Z.; Wang, H.; Huang, H.; Cao, C. Photocatalysis Enhancement By Electric Field: TiO_2 Thin Film For Degradation of Dye X-3B, *Chemosphere* **2004**, *56*, 503-508

(8) Tank, C. M.; Sakhare, Y. S.; Kanhe, N. S.; Nawale, A. B.; Das, A. K.; Bhoraskar, S. V.; Mathe, V. L. Electric Field Enhanced Photocatalytic Properties of TiO_2 Nanoparticles Immobilized in Porous Silicon Template, *Solid State Sci.* **2011**, *13*, 1500-1504

(9) Zhang, Z.; Yates, J. T. Effect of Adsorbed Donor and Acceptor Molecules on Electron Stimulated Desorption: $O_2/TiO_2(110)$, *J. Phys. Chem. Lett.* **2010**, *1*, 2185-2188

(10) Kaneko, M.; Okura, I. *Photocatalysis: Science and Technology*; Kaneko, M.; Okura, I., Eds.; Springer: Heidelberg, 2002.

(11) Fujihara, K.; Izumi, S.; Ohno, T.; Matsumura, M. Time-Resolved Photoluminescence of Particulate TiO_2 Photocatalysts Suspended in Aqueous Solutions, *J. Photoch. Photobio. A* **2000**, *132*, 99-104

(12) Schierbaum, K. D.; Weimar, U.; Göpel, W.; Kowalkowski, R. Conductance, Work Function and Catalytic Activity of SnO_2-Based Gas Sensors, *Sensor Actuator* **1991**, *3*, 205-214

(13) Ohno, T.; Haga, D.; Fujihara, K.; Kaizaki, K.; Matsumura, M. Unique Effects of Iron(III) Ions on Photocatalytic and Photoelectrochemical Properties of Titanium Dioxide, *J. Phys. Chem. B* **1997**, *101*, 6415-6419

(14) Wilson, J. N.; Idriss, H. Effect of Surface Reconstruction of TiO_2(001) Single Crystal on the Photoreaction of Acetic Acid, *J. Catal.* **2003**, *214*, 46-52

(15) Wilson, J. N.; Idriss, H. Structure Sensitivity and Photocatalytic Reactions of Semiconductors. Effect of the Last Layer Atomic Arrangement, *J. Am. Chem. Soc.* **2002**, *124*, 11284-11285

(16) Liu, G.; Wang, L.; Yang, H. G.; Cheng, H.-M.; Lu, G. Q. Titania-Based Photocatalysts - Crystal Growth, Doping and Heterostructuring, *J. Mater. Chem.* **2010**, *20*, 831-843

(17) Linsebigler, A. L.; Lu, G.; Yates, J. T. Photocatalysis on TiO_2 Surfaces: Principles, Mechanisms, and Selected Results, *Chem. Rev.* **1995**, *95*, 735-758

(18) Sellers, M. C. K.; Seebauer, E. G. Manipulation of Polycrystalline TiO_2 Carrier Concentration via Electrically Active Native Defects, *J. Vac. Sci. Technol. A* **2011**, *29*, 061503-061508

(19) Seebauer, E. G.; Kratzer, M. C. Charged Point Defects in Semiconductors, *Mater. Sci. Eng. R* **2006**, *55*, 57-149

(20) Seebauer, E. G.; Kratzer, M. C. *Charged Semiconductor Defects: Structure, Thermodynamics and Diffusion*; Springer: London, 2009.

(21) Seebauer, E. G.; Noh, K. W. Trends in Semiconductor Defect Engineering at the Nanoscale, *Mater. Sci. Eng. R* **2010**, *70*, 151-168

(22) Nowotny, M. K.; Sheppard, L. R.; Bak, T.; Nowotny, J. Defect Chemistry of Titanium Dioxide. Application of Defect Engineering in Processing of TiO_2-Based Photocatalyststst, *J. Phys. Chem. C* **2008**, *112*, 5275-5300

(23) Ozawa, K.; Emori, M.; Yamamoto, S.; Yukawa, R.; Yamamoto, S.; Hobara, R.; Fujikawa, K.; Sakama, H.; Matsuda, I. Electron–Hole Recombination Time at TiO_2 Single-Crystal Surfaces: Influence of Surface Band Bending, *J. Phys. Chem. Lett.* **2014**, *5*, 1953-1957

(24) Hashimoto, K.; Irie, H.; Fujishima, A. TiO_2 Photocatalysis: A Historical Overview and Future Prospects, *Jpn. J. Appl. Phys.* **2005**, *44*, 8269

(25) Linsebigler, A.; Lu, G.; Yates, J. J. T. CO Chemisorption on TiO_2 (110): Oxygen Vacancy Site Influence on CO Adsorption, *J. Chem. Phys.* **1995**, *103*, 9438-9443

(26) Vaseashta, A.; Vaclavikova, M.; Vaseashta, S.; Gallios, G.; Roy, P.; Pummakarnchana, O. Nanostructures in Environmental Pollution Detection, Monitoring, and Remediation, *Sci. Technol. Adv. Mat.* **2007**, *8*, 47-59

(27) Augugliaro, V.; Coluccia, S.; Loddo, V.; Marchese, L.; Martra, G.; Palmisano, L.; Pantaleone, M.; Schiavello, M. VOC's Abatement: Photocatalytic Oxidation of Toluene in Vapour Phase on Anatase TiO_2 Catalyst, *Stud. Surf. Sci. Catal.* **1997**, *110*, 663-672

(28) Hosseini, M.; Tidahy, H. L.; Siffert, S.; Cousin, R.; Abouka ъ, A.; Su, B. L. Effects of the Treatment and the Mesoporosity of Mesostructured TiO_2 Impregnated with Noble Metal for VOCs Oxidation, *Stud. Surf. Sci. Catal.* **2008**, *Volume 174, Part B*, 1323-1326

(29) Papaefthimiou, P.; Ioannides, T.; Verykios, X. E. Performance of Doped Pt/TiO_2 (W^{6+}) Catalysts for Combustion of Volatile Organic Compounds (VOCs), *Appl. Catal. B-Environ.* **1998**, *15*, 75-92

(30) Lakshmi, S.; Renganathan, R.; Fujita, S. Study on TiO_2-Mediated Photocatalytic Degradation of Methylene Blue, *J. Photoch. Photobio. A* **1995**, *88*, 163-167

(31) Zhang, T.; Oyama, T.; Aoshima, A.; Hidaka, H.; Zhao, J.; Serpone, N. Photooxidative N-Demethylation of Methylene Blue in Aqueous TiO_2 Dispersions under UV Irradiation, *J. Photoch. Photobio. A* **2001**, *140*, 163-172

(32) Houas, A.; Lachheb, H.; Ksibi, M.; Elaloui, E.; Guillard, C.; Herrmann, J.-M. Photocatalytic Degradation Pathway of Methylene Blue in Water, *Appl. Catal. B-Environ.* **2001**, *31*, 145-157

(33) Kapinus, E.; Viktorova, T. Kinetics of the Photocatalytic Degradation of Methylene Blue on Titanium Dioxide, *Theor. Exp. Chem.* **2010**, *46*, 163-167

(34) Kuo, W. S.; Ho, P. H. Solar Photocatalytic Decolorization of Methylene Blue in Water, *Chemosphere* **2001**, *45*, 77-83

(35) Ling, C. M.; Mohamed, A. R.; Bhatia, S. Performance of Photocatalytic Reactors Using Immobilized TiO_2 Film for the Degradation of Phenol and Methylene Blue Dye Present in Water Stream, *Chemosphere* **2004**, *57*, 547-554

(36) Matthews, R. W. Photocatalytic Oxidation and Adsorption of Methylene Blue on Thin Films of Near-Ultraviolet-Illuminated TiO_2, *J. Chem. Soc. Farad. T. 1* **1989**, *85*, 1291-1302

(37) Mills, A. An Overview of the Methylene Blue ISO Test for Assessing the Activities of Photocatalytic Films, *Appl. Catal. B-Environ.* **2012**, *128*, 144-149

(38) Tennakone, K.; Senadeera, S.; Priyadharshana, A. TiO_2 Catalysed Photo-Oxidation of Water in the Presence of Methylene Blue, *Sol. Energ. Mat. Sol. C.* **1993**, *29*, 109-113

(39) Yu, Z.; Chuang, S. S. C. Probing Methylene Blue Photocatalytic Degradation by Adsorbed Ethanol with In Situ IR, *J. Phys. Chem. C* **2007**, *111*, 13813-13820

(40) Wu, C.-H.; Chern, J.-M. Kinetics of Photocatalytic Decomposition of Methylene Blue, *Ind. Eng. Chem. Res.* **2006**, *45*, 6450-6457

(41) Sellers, M. C. K.; Seebauer, E. G. Measurement Method for Carrier Concentration in TiO_2 via the Mott–Schottky Approach, *Thin Solid Films* **2011**, *519*, 2103-2110

(42) Streetman, B. G.; Banerjee, S. K. *Solid State Electronic Devices*; Prentice-Hall: Upper Sadle River, 2006.

(43) Butler, M. A. Photoelectrolysis and Physical Properties of the Semiconducting Electrode WO_2, *J. Appl. Phys.* **1977**, *48*, 1914-1920

(44) Henrich, V. E.; Cox, P. A. *The Surface Science of Metal Oxides*; Cambridge University Press: New York, 1994.

(45) Kaneko, H.; Miyake, K. Physical Properties of Antimony-Doped Tin Oxide Thick Films, *J. Appl. Phys.* **1982**, *53*, 3629-3633

(46) Windisch, J. C. F.; Exarhos, G. J. Mott--Schottky Analysis of Thin ZnO Films, *J. Vac. Sci. Technol. A* **2000**, *18*, 1677-1680

(47) Lu, H.; Schaff, W. J.; Eastman, L. F.; Wu, J.; Walukiewicz, W.; Look, D. C.; Molnar, R. J. Growth of Thick InN by Molecular Beam Epitaxy, *MRS Proceedings* **2002**, *743*, L4.10

(48) Nowotny, J.; Bak, T.; Burg, T.; Nowotny, M. K.; Sheppard, L. R. Effect of Grain Boundaries on Semiconducting Properties of TiO_2 at Elevated Temperatures, *J. Phys. Chem. C* **2007**, *111*, 9769-9778

(49) Tada, H.; Tanaka, M. Dependence of TiO_2 Photocatalytic Activity upon Its Film Thickness, *Langmuir* **1997**, *13*, 360-364

(50) Nam, H. J.; Amemiya, T.; Murabayashi, M.; Itoh, K. Photocatalytic Activity of Sol−Gel TiO_2 Thin Films on Various Kinds of Glass Substrates: The Effects of Na^+ and Primary Particle Size, *J. Phys. Chem. B* **2004**, *108*, 8254-8259

(51) Yoshida, K.; Okamura, K.; Itoh, K.; Murabayashi, M. Photocatalytic Degradation of Chlorinated Compounds in Water. Effect of the Number of the Repeated Dip-Coating for the TiO_2 Thin-Film on the degradation of TCE., *Denki Kagaku* **1998**, *66*, 171

(52) Eufinger, K.; Poelman, D.; Poelman, H.; De Gryse, R.; Marin, G. B. TiO_2 Thin Films for Photocatalytic Applications. In *Thin Solid Films: Process and Applications*; Nam, S. C., Ed.; Transworld Research Network: Kerala, India, 2008, pp 189-227.

(53) Jung, S. C.; Kim, S. J.; Imaishi, N.; Cho, Y. I. Effect Of TiO_2 Thin Film Thickness and Specific Surface Area by Low-Pressure Metal–Organic Chemical Vapor Deposition on Photocatalytic Activities, *Appl. Catal. B-Environ.* **2005**, *55*, 253-257

(54) Salvador, P. The Influence of Niobium Doping on the Efficiency of n-TiO_2 Electrode in Water Photoelectrolysis, *Sol. Energ. Mater.* **1980**, *2*, 413-421

(55) Epling, G. A.; Lin, C. Photoassisted Bleaching of Dyes Utilizing TiO_2 and Visible Light, *Chemosphere* **2002**, *46*, 561-570

(56) Boschloo, G. K.; Goossens, A.; Schoonman, J. Photoelectrochemical Study of Thin Anatase TiO_2 Films Prepared by Metallorganic Chemical Vapor Deposition, *J. Electrochem. Soc.* **1997**, *144*, 1311-1317

(57) Park, Y. R.; Kim, K. J. Structural and Optical Properties of Rutile and Anatase TiO_2 Thin Films: Effects of Co Doping, *Thin Solid Films* **2005**, *484*, 34-38

(58) Sumita, T.; Yamaki, T.; Yamamoto, S.; Miyashita, A. Photo-Induced Surface Charge Separation of Highly Oriented TiO_2 Anatase and Rutile Thin Films, *Appl. Surf. Sci.* **2002**, *200*, 21-26

(59) Hasan, M. M.; Haseeb, A. S. M. A.; Saidur, R.; Masjuki, H. H. Effects of Annealing Treatment on Optical Properties of Anatase TiO_2 Thin Films, *World Acad. Sci. Eng. Technol.* **2008**, *40*, 221-225

(60) Aarik, J.; Aidla, A.; Kiisler, A.-A.; Uustare, T.; Sammelselg, V. Effect of Crystal Structure on Optical Properties of TiO_2 Films Grown by Atomic Layer Deposition, *Thin Solid Films* **1997**, *305*, 270-273

(61) Johnson, E. J. Absorption near the Fundamental Edge. In *Semiconductors and Semimetals*; Willardson, R. K., Beer, A., C. , Eds.; Academic Press: 1967; Vol. 3, pp 153-258.

(62) Watanabe, Y.; Muramoto, Y.; Shimizu, N. In *Electronic Conduction Properties of TiO_2 Thin Films under UV Light Irradiation*, 2011 Annual Report Conference on Electrical Insulation and Dielectric Phenomena, Cancun, Mexico, 16-19 Oct. 2011, IEEE, 2011

(63) Enache, C.; Schoonman, J.; Krol, R. The Photoresponse of Iron- and Carbon-Doped TiO_2 (Anatase) Photoelectrodes, *J. Electroceram.* **2004**, *13*, 177-182

(64) Tang, H.; Prasad, K.; Sanjines, R.; Schmid, P. E.; Levy, F. Electrical and Optical Properties of TiO_2 Anatase Thin Films, *J. Appl. Phys.* **1994**, *75*, 2042-2047

(65) Yamada, Y.; Kanemitsu, Y. Determination of Electron and Hole Lifetimes of Rutile and Anatase TiO_2 Single Crystals, *Appl. Phys. Lett.* **2012**, *101*, 133907

(66) Sham, T. K.; Lazarus, M. S. X-Ray Photoelectron Spectroscopy (XPS) Studies of Clean and Hydrated TiO_2 (Rutile) Surfaces, *Chem. Phys. Lett.* **1979**, *68*, 426-432

(67) Wang, L. Q.; Baer, D. R.; Engelhard, M. H.; Shultz, A. N. The Adsorption of Liquid and Vapor Water on TiO_2(110) Surfaces: The Role of Defects, *Surf. Sci.* **1995**, *344*, 237-250

(68) Erdem, B.; Hunsicker, R. A.; Simmons, G. W.; Sudol, E. D.; Dimonie, V. L.; El-Aasser, M. S. XPS and FTIR Surface Characterization of TiO_2 Particles Used in Polymer Encapsulation, *Langmuir* **2001**, *17*, 2664-2669

(69) Jensen, H.; Soloviev, A.; Li, Z.; Søgaard, E. G. XPS and FTIR Investigation of the Surface Properties of Different Prepared Titania Nano-Powders, *Appl. Surf. Sci.* **2005**, *246*, 239-249

(70) Fujishima, A.; Rao, T. N.; Tryk, D. A. Titanium Dioxide Photocatalysis, *J. Photoch. Photobio. C* **2000**, *1*, 1-21

(71) Zheng, W.; Wei, H.; Cheng, L.; Lai, H.; Songyan, C. Modulation of Schottky Barrier Height of Metal/TaN/n-Ge Junctions by Varying TaN Thickness, *IEEE T. Electron. Dev.* **2012**, *59*, 1328-1331

(72) Jiang, Y. L.; Xie, Q.; Qu, X. P.; Ru, G. P.; Zhang, D. W.; Deduytsche, D.; Detavernier, C. Effective Schottky Barrier Height Modulation by an Ultrathin Passivation Layer of GeOxNy for Al/n-Ge(100) Contact, *Electrochem. Solid St.* **2011**, *14*, H487-H490

(73) Tomonori, N.; Koji, K.; Akira, T. A Significant Shift of Schottky Barrier Heights at Strongly Pinned Metal/Germanium Interface by Inserting an Ultra-Thin Insulating Film, *Appl. Phys. Express* **2008**, *1*, 051406

(74) Albery, W. J.; Bartlett, P. N. The Transport and Kinetics of Photogenerated Carriers in Colloidal Semiconductor Electrode Particles, *J. Electrochem. Soc.* **1984**, *131*, 315-325

(75) Le Dréo, H.; Banakh, O.; Keppner, H.; Steinmann, P. A.; Briand, D.; de Rooij, N. F. Optical, Electrical and Mechanical Properties of the Tantalum Oxynitride Thin Films Deposited by Pulsing Reactive Gas Sputtering, *Thin Solid Films* **2006**, *515*, 952-956

(76) Takata, T.; Hitoki, G.; Kondo, J. N.; Hara, M.; Kobayashi, H.; Domen, K. Visible-Light-Driven Photocatalytic Behavior of Tantalum-Oxynitride and Nitride, *Res. Chem. Intermed.* **2007**, *33*, 13-25

(77) Higashi, M.; Domen, K.; Abe, R. Highly Stable Water Splitting on Oxynitride TaON Photoanode System under Visible Light Irradiation, *J. Am. Chem. Soc.* **2012**, *134*, 6968-6971

(78) Nada, A. A.; Barakat, M. H.; Hamed, H. A.; Mohamed, N. R.; Veziroglu, T. N. Studies on the Photocatalytic Hydrogen Production Using Suspended Modified Photocatalysts, *Int. J. Hydrogen Energ.* **2005**, *30*, 687-691

(79) Li, Y.; Lu, G.; Li, S. Photocatalytic Production of Hydrogen in Single Component and Mixture Systems of Electron Donors and Monitoring Adsorption of Donors by In Situ Infrared Spectroscopy, *Chemosphere* **2003**, *52*, 843-850

(80) Nisar, J.; Wang, B.; Araujo, C. M.; Ferreira da Silva, A.; Kang, T. W.; Ahuja, R. Band Gap Engineering by Anion Doping in the Photocatalyst $BiTaO_4$: First Principle Calculations, *Int. J. Hydrogen Energ.* **2012**, *37*, 3014-3018

(81) Anandan, S.; Ohashi, N.; Miyauchi, M. ZnO-based visible-light photocatalyst: Band-gap engineering and multi-electron reduction by co-catalyst, *Appl. Catal. B-Environ.* **2010**, *100*, 502-509

(82) Wang, B. C.; Nisar, J.; Pathak, B.; Kang, T. W.; Ahuja, R. Band Gap Engineering In $BiNbO_4$ for Visible-Light Photocatalysis, *Appl. Phys. Lett.* **2012**, *100*, -

(83) Jones, E. C.; Ishida, E. Shallow Junction Doping Technologies for ULSI, *Mater. Sci. Eng. R* **1998**, *24*, 1-80

(84) Gossmann, H. L. Junction Formation and Its Device Impact Through the Nodes: From Single to Coimplants, From Beam Line to Plasma, From Single Ions to Clusters, and from Rapid Thermal Annealing to Laser Thermal Processing, *J. Vac. Sci. Technol. B* **2008**, *26*, 267-272

(85) Sinno, T.; Dornberger, E.; von Ammon, W.; Brown, R. A.; Dupret, F. Defect Engineering of Czochralski Single-Crystal Silicon, *Mater. Sci. Eng. R* **2000**, *28*, 149-198

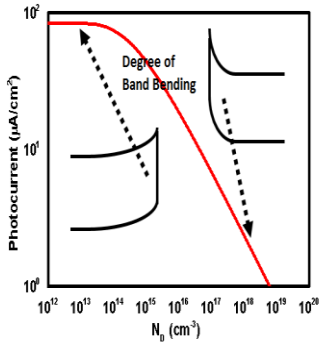
Degree of
Band Bending
Photocurrent (μA/cm²)
10²
10¹
10⁰
10¹² 10¹³ 10¹⁴ 10¹⁵ 10¹⁶ 10¹⁷ 10¹⁸ 10¹⁹ 10²⁰
N_D (cm⁻³)